Lars Kiewidt, Jorg Thöming

# Predicting optimal temperature profiles in single-stage fixed-bed reactors for CO2-methanation

| | | |
|---|---|---|
| Journal Article | as: | peer-reviewed accepted version (Postprint) |
| DOI of this document*(secondary publication): | | https://doi.org/10.26092/elib/2458 |
| Publication date of this document: | | 11/09/2023 |

* for better findability or for reliable citation

Recommended Citation (primary publication/Version of Record) incl. DOI:

Lars Kiewidt, Jorg Thöming,
Predicting optimal temperature profiles in single-stage fixed-bed reactors for CO2-methanation,
Chemical Engineering Science, Volume 132, 2015, Pages 59-71, ISSN 0009-2509,
https://doi.org/10.1016/j.ces.2015.03.068

# Predicting optimal temperature profiles in single-stage fixed-bed reactors for $CO_2$-methanation

Lars Kiewidt *, Jorg Thöming **

*Center for Environmental Research and Sustainable Technology (UFT), University of Bremen, Leobener Straße, 28359 Bremen, Germany*

## HIGHLIGHTS

- We present a method to compute optimal temperature profiles in fixed-bed reactors.
- We predict optimal temperature profiles for the methanation of $CO_2$.
- These temperature profiles result in a twofold improvement of the methane-yield.
- The results demonstrate the potential of improved heat transport in catalyst supports.

## GRAPHICAL ABSTRACT

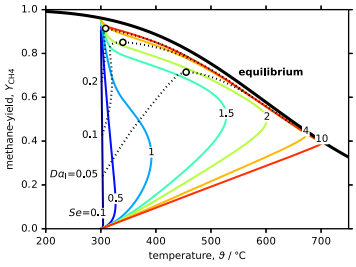


## ARTICLE INFO

*Article history:*
Received 5 December 2014
Received in revised form
2 March 2015
Accepted 29 March 2015
Available online 13 April 2015

*Keywords:*
Methanation
Thermal optimization
Process intensification
Chemical energy storage
Semenov number

## ABSTRACT

The catalytic conversion of carbon dioxide into methane, known as Sabatier process, is a promising option for chemical storage of excess renewable energy and greenhouse gas emission control. Typically externally cooled fixed-bed reactors (FBR) using supported nickel or ruthenium catalyst are applied. The Sabatier process, however, is strongly exothermic and leads to substantial hot spots within the reactor at stoichiometric feed ratios. Although high temperatures increase the reaction rate in general, they thermodynamically limit the achievable methane-yield in the Sabatier process. Here, we present an easy-to-use method based on a Semenov number optimization (SNO) to compute optimal axial temperature profiles in single-stage fixed-bed reactors that account for kinetic and thermodynamic limitations simultaneously, and thus result in maximized yield for a fixed reactor length. In a case study on $CO_2$-methanation, these temperature profiles result in a twofold improvement of the methane-yield compared to isothermal and adiabatic operation, and thus demonstrate the high potential of thermal optimization that lies in the Sabatier process. The SNO-method provides a valuable tool to compute optimal temperature profiles, and allows intuitive insight into the key parameters for thermal process intensification. Further, it can readily be transferred to other processes that suffer from the dilemma between kinetic and thermodynamic limitations. Our findings illustrate the attractiveness of the SNO-method to compute optimal temperature profiles in fixed-bed reactors, and the need for catalyst supports with enhanced and tailorable heat transport properties.

## 1. Introduction

The catalytic hydrogenation of carbon dioxide ($CO_2$) to methane ($CH_4$), or substitute natural gas (SNG), is already known for more than 100 years since the fundamental work of Sabatier and Senderens (1902). Nevertheless, research and industry mainly focused on selective methanation of carbon monoxide (CO) to

* Corresponding author. Tel.: +49 421 218 63388.
** Principal Investigator.
*E-mail addresses:* kiewidt@uni-bremen.de (L. Kiewidt), thoeming@uni-bremen.de (J. Thöming).

http://dx.doi.org/10.1016/j.ces.2015.03.068

purify hydrogen-rich feed streams ($CO \leq 1$ vol%) for ammonia-synthesis and, more recently, fuel cell applications (Park et al., 2009; Krämer et al., 2007; Batista et al., 2005). In the 1970s increasing natural gas prices intensified the efforts for coal-based SNG production and led to a commercial plant in the United States. Kopyscinski et al. (2010) and Sudiro et al. (2010) give comprehensive reviews of the history of SNG production and past and modern realizations of the $CO_2$/CO-methanation process.

Nowadays, catalytic methanation of $CO_2$, also known as Sabatier process, is frequently discussed as promising candidate for $CO_2$-utilization and grid-scale Chemical Energy Storage via hydrogen ($H_2$) from electrolysis using excess renewable energy (Power-to-Gas, PtG) (Schlögl, 2013; Centi et al., 2013; Centi and Perathoner, 2009). Minutillo and Perna (2014) and Hoekman et al. (2010) investigated the methanation of $CO_2$ particularly in the framework of Chemical Energy Storage. Jürgensen et al. (2014) presented a scenario for SNG-based Chemical Energy Storage for northern Germany based on the Sabatier process. A similar scenario was also presented by Moeller et al. (2014) for Germany's capital region Berlin-Brandenburg. Further, Mohseni et al. (2013) evaluated the economic potential of SNG-based Chemical Energy Storage in Sweden.

Bassano et al. (2013), Gnanamani et al. (2014), and Wang et al. (2011, 2010) provide detailed reviews on $CO_2$-methanation from a technical viewpoint regarding catalysts, mechanisms, and reactor aspects. The $CO_2$-methanation, commonly summarized as

$$CO_2 + 4\,H_2 \leftrightarrows CH_4 + 2\,H_2O, \quad \Delta H_R^{298} = -165\ \text{kJ mol}^{-1}, \tag{1}$$

is typically performed in fixed-bed reactors at increased pressures up to 20 bar (2 MPa) and feed temperatures between 250 °C and 400 °C. Usually supported nickel (Ni) and ruthenium (Ru) catalysts are applied because of kinetic limitations at low temperatures. The main challenge at undiluted stoichiometric molar feed ratios of $H_2$:$CO_2$=4:1 is the strong exothermicity of the reaction that leads to high temperatures within the reactor if it is not properly cooled. We note that this is not the case in selective methanation of CO for purification because of the low CO concentrations. Although high temperatures are generally favorable from a kinetic point of view, they induce thermodynamic limitations in the Sabatier process and limit the achievable methane-yield. In addition, too high temperatures accelerate catalyst deactivation by thermal sintering and thus reduce catalyst lifetime.

Fig. 1 shows the equilibrium $CO_2$-conversion, methane-yield, and gas composition for various temperatures in a Sabatier process at atmospheric pressure. The curves are computed from ideal gas phase thermodynamics using a stoichiometric method described by, among others, Leal et al. (2013). A more detailed thermodynamic study of the Sabatier process, including impurities of the feed, was conducted by Gao et al. (2012). In Fig. 1a, the methane-yield decreases monotonically with increasing temperature and the $CO_2$-conversion exhibits a minimum around 600 °C because the inverse reaction, known as methane steam reforming, becomes thermodynamically favorable. At temperatures higher than 600 °C CO-formation via the reverse water-gas shift (RWGS) reaction is significant (Fig. 1b), and thus the overall $CO_2$-conversion increases again. Nevertheless, methane-yield remains low at high temperatures.

In order to face the high exothermicity of the Sabatier reaction and obtain high methane-yields several reactor concepts have been proposed in the past. Brooks et al. (2007), Liu et al. (2012) and Hu et al. (2007) used microchannel reactors ($D_t \leq 1$ mm), which provide large volumetric surface areas, to efficiently remove the reaction heat. This type of reactor, however, allows only capacities and is thus better suited for mobile and small-scale applications than for grid-scale Chemical Energy Storage.

Sudiro et al. (2010) theoretically investigated massive metallic honeycomb-type structures to improve lateral heat transport in externally cooled multitubular reactors for the methanation of a 1:1 $CO/CO_2$ mixture in 60% $H_2$. They reported single-pass CO-conversions up to 80% and an temperature rise from 300 °C to approximately 550 °C.

Schlereth and Hinrichsen (2014) conducted a detailed computational study of the Sabatier process in externally cooled fixed-bed reactors (FBR) including one- and two-dimensional simulations. They predicted considerable hot spots in conventional FBRs and proposed a membrane reactor to feed $CO_2$ separately along the reactor axis and thus control the heat release locally. Ohya et al. (1997) already used a membrane reactor for the $CO_2$-methanation several years ago, however, they primarily intended to remove water from the reaction zone to suppress the reverse reaction.

Schaaf and Grünig (2014) employed a cascaded Sabatier process with several adiabatic reaction and subsequent cooling stages to obtain high methane-yields. Additionally, they recycled some of the product gas from the first stage to dilute the reactants and absorb part of the reaction heat. Depending on the feed, a 50 vol% $CO_2/CH_4$ mixture from biomass or pure $CO_2$, they employed 2–4 sequential reaction-cooling stages to keep the maximum temperature below 550 °C and obtain $CO_2$-conversions up to 70%.

A more involved approach to deal with the exothermicity is to acutely control the temperature profile along the reactor axis and utilize part of the reaction heat for accelerated kinetics. Smets et al. (2002) and Logist et al. (2008) followed this approach and

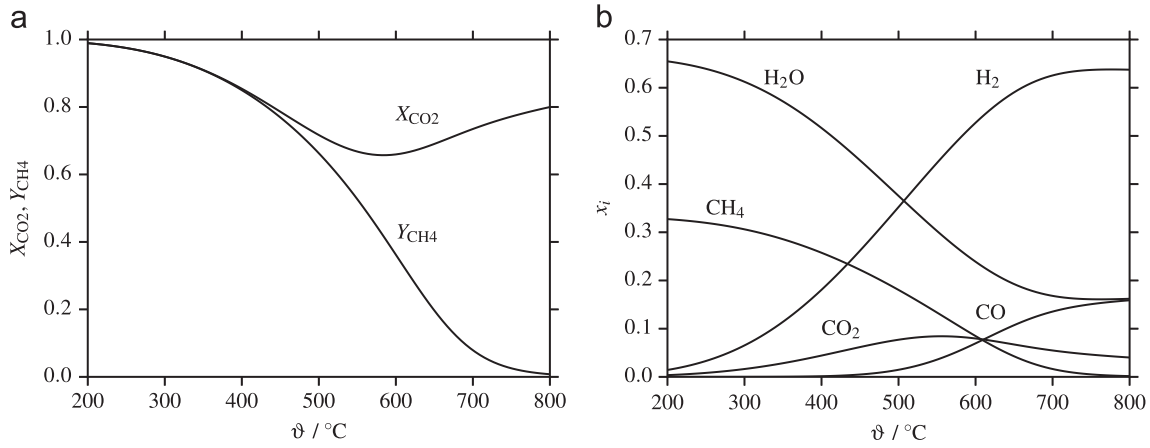


**Fig. 1.** (a) Equilibrium $CO_2$-conversion and methane-yield, and (b) equilibrium composition of a Sabatier process, as a function of the temperature at $p$=1 bar (0.1 MPa) and stoichiometric molar feed ratio $H_2 : CO_2 = 4 : 1$.

computed optimal temperature profiles in tubular reactors to maximize the conversion of generic first-order exothermic reactions by optimizing the cooling-temperature profile along the reactor axis. Freund and Sundmacher (2008) and Peschel et al. (2010) developed a universal methodology for the optimization of chemical reactors. They predicted optimal temperature profiles for the thermodynamically limited $SO_2$-oxidation process, and proposed a cascaded reactor network of three stages to realize an approximation of their predicted temperature profile. This classic technical solution for thermodynamically limited processes, however, requires a substantial amount of equipment and accessory and is consequently more suited for centralized large-scale plants, where economy of scale shifts the economic optimum towards higher capital costs, than for local, distributed Chemical Energy Storage.

In this study we demonstrate a new and easy-to-use method that utilizes a simple one-dimensional, pseudo-homogeneous reactor model and the *Semenov number*, commonly applied in the field of parametric sensitivity and reactor safety (Varma et al., 2005), to predict optimal temperature profiles in externally cooled, *single-stage* FBRs. The method is based on the optimization of the Semenov number and is thus referred to as *Semenov-number-optimization* (*SNO*)-*method* in the following. We apply the SNO-method, which accounts for kinetic and thermodynamic limitations simultaneously, to predict optimal axial temperature profiles in an externally cooled, single-stage FBRs using the Sabatier process as a case study.

In Section 2 we describe the pseudo-homogeneous model and the numerical solution algorithm. Further, the model is validated using experimental data reported in the literature. In Section 3 we explain the concept of optimal Semenov numbers and compute tailored temperature profiles for the Sabatier process. Subsequently, we investigate the feasibility of these temperature profiles in a case study and discuss the results. Finally, we conclude our findings in Section 4 and provide an outlook for future research.

## 2. The pseudo-homogeneous fixed-bed reactor model and the SNO-method

### 2.1. Description of the dimensional model

#### 2.1.1. Mass, momentum, and energy balances

To study the $CO_2$-methanation process we employ a pseudo-homogeneous plug-flow reactor (PFR) model based on well-established balance equations for mass, momentum, concentration, and energy (Bird et al., 2007; Froment et al., 2011, Section 11.5 and Chapter 19, respectively). The class of pseudo-homogeneous models combines the fluid and solid phase within the reactor to a single effective phase and thus neglects interfacial heat and mass transfer. Internal transport is usually considered by effectiveness factors computed with single-pellet models. Fig. 2 shows a schematic of an externally cooled, single-stage FBR as considered in this study.

The corresponding balance equations for mass, momentum, concentration, and energy within in the catalyst bed read

$$\frac{\mathrm{d}G}{\mathrm{d}z} = 0 \tag{2a}$$

$$\frac{\mathrm{d}p}{\mathrm{d}z} = -\frac{\mu}{K}\frac{G}{\rho} - \frac{\rho}{c_\mathrm{F}}\left(\frac{G}{\rho}\right)^2 \tag{2b}$$

$$G\frac{\mathrm{d}\omega_i}{\mathrm{d}z} = M_i \sum_{j=1}^{n_r} \nu_{ij}\eta_j r_j^{(V)}, \quad i = 1\ldots n_\mathrm{s} \tag{2c}$$

$$Gc_\mathrm{p}\frac{\mathrm{d}T}{\mathrm{d}z} = \sum_{j=1}^{n_r} (-\Delta H_R)_j \eta_j r_j^{(V)} + \frac{4U_\mathrm{w}^{(\mathrm{eff})}}{D_\mathrm{R}}(T - T_\mathrm{c}), \tag{2d}$$

subject to Dirichlet boundary conditions at the entrance of the catalyst bed at $z=0$:

$$G(z=0) = G_0 \tag{3a}$$

$$p(z=0) = p_0 \tag{3b}$$

$$\omega_i(z=0) = \omega_{i,0} \tag{3c}$$

$$T(z=0) = T_0. \tag{3d}$$

Here, $G = \rho\varepsilon v_z$ is the gas load that remains constant along the reactor because of mass conservation. The pressure loss due to the packed bed is modeled by a Darcy–Forchheimer type expression in Eq. (2b); the cooling rate at the wall of the catalyst bed in Eq. (2d) is described by Newton's law of cooling. Explicit expressions for the reaction rate, $r_j^{(V)}$, the effectiveness factor, $\eta_j$, the Darcy–Forchheimer coefficients, $K$ and $c_\mathrm{F}$, and the effective wall heat transfer coefficient, $U_\mathrm{w}^{(\mathrm{eff})}$, are given in the following subsections.

Eqs. (2a)–(2d) are complemented by an equation of state, here for an ideal gas, to link pressure, temperature, and density within the reactor:

$$p = \frac{\rho R_\mathrm{u} T}{M}. \tag{4}$$

The overall performance of the reactor is evaluated by the $CO_2$-conversion, $X_{CO_2}$, the methane-yield, $Y_{CH_4}$, and the volumetric space–time yield, *STY*:

$$X_{CO_2} = \frac{\dot{n}_{CO_2,0} - \dot{n}_{CO_2}}{\dot{n}_{CO_2,0}} \tag{5a}$$

$$Y_{CH_4} = \frac{\dot{n}_{CH_4} - \dot{n}_{CH_4,0}}{\dot{n}_{CO_2,0}} \tag{5b}$$

$$STY = \frac{\dot{m}_{CH_4,\mathrm{out}}}{V_\mathrm{R}}. \tag{5c}$$

We note that the set of ordinary differential equations (2a)–(2d) (ODE) results from major simplifications of the full set of partial

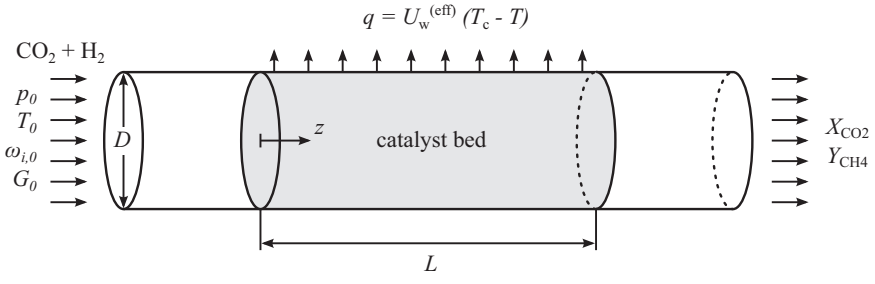


**Fig. 2.** Sketch of the single-stage externally cooled FBR considered in this study.

differential equations (PDE) for an externally cooled FBR: firstly, we neglect any transient changes in the dependent variables as the boundary conditions do not vary in time; secondly, we do not consider axial dispersion of mass or energy because convective transport is assumed to be much larger than the dispersive contribution; thirdly, we do not explicitly include radial changes of the dependent variables, however, radial heat transport is modeled by the effective wall heat transfer coefficient, $U_w^{(eff)}$, as explained by Rasmuson et al. (2014, Section 5.2.5). Therefore we emphasize that the dependent variables in Eqs. (2a)–(2d) represent cross-sectional averages of the radially distributed dependent variables.

Nevertheless, we use the pseudo-homogeneous, one-dimensional approach to investigate the Sabatier process because it provides a good compromise between computational costs and physical accuracy for the kinetics and parameter range considered in this study. The applicability of a pseudo-homogeneous model was also confirmed by Schlereth and Hinrichsen (2014) and Parlikkad et al. (2013) for a Sabatier process at similar conditions. In general, the validity of a one-dimensional pseudo-homogeneous model should be justified by *Mears' criteria*, as presented in Section 2.4.

#### 2.1.2. Description of the kinetic model

Here, we use the kinetic model of Lunde and Kester (1974) who consider solely the global methanation reaction of $CO_2$, Eq. (1), on a 0.5 wt% Ru-catalyst in their kinetic model. They state that the reverse-water-gas-shift (RWGS) reaction and subsequent CO-methanation may also occur simultaneously, however, the latter proceeds rapidly at typical reaction conditions, and therefore it is valid to consider only the global reaction. Further, CO-formation via the RWGS reaction is thermodynamically limited below 650 °C for a $CO_2/H_2$-feed at 10 bar (1 MPa). Only after the $CO_2$-methanation produced a substantial amount of heat, and thus consumed a major fraction of $CO_2$, a small fraction of CO is formed that is converted to $CH_4$. Consequently, the use of the global reaction, Eq. (1), will give a good approximation of the hot spot for the considered conditions. In addition, the detailed reaction mechanism of the $CO_2$-methanation is still ambiguous as outlined by Gnanamani et al. (2014, pp. 100f.).

In their work, Lunde and Kester (1974) used an apparent reaction order $n$ to fit the reaction rate of the global $CO_2$-methanation reaction on a 0.5 wt% Ru catalyst, stabilized on cylindrical 3.2 mm by 3.2 mm alumina pellets, to a gas-phase reaction model. Their final expression for the volumetric reaction rate, $r^{(V)}$, reads

$$r^{(V)} = A \exp\left\{-\frac{E_a}{R_u T}\right\} \left(p_{CO_2}^n p_{H_2}^{4n} - \frac{1}{K_p^n} p_{CH_4}^n p_{H_2O}^{2n}\right) \tag{6}$$

with $n = 0.225$, $A = 4.906 \times 10^5\ s^{-1}\ bar^{-0.125}$, and $E_a = 70.52$ kJ mol$^{-1}$. The reverse reaction is modeled by the equilibrium constant in pressure form, $K_p$, that is computed from ideal equilibrium gas-phase thermodynamics.

Lunde and Kester (1974) also state that the catalyst was localized only on the outer surface of the alumina pellets and thus internal transport limitations were negligible in their experiments. Consequently, Eq. (6) models the intrinsic reaction rate.

Ohya et al. (1997) used the same model to describe the reaction rate of the global $CO_2$-methanation reaction on an equivalent catalyst and obtained a similar activation energy and pre-exponential factor but found $n = 0.85$. Later Brooks et al. (2007) referred to the model of Lunde and Kester (1974) to fit the kinetics of a 3 wt% $Ru/TiO_2$ catalyst in powder form ($d_p \approx 250$ µm). They obtained similar values for the activation energy and catalyst coefficient, however, their reported model is slightly different and thus not directly comparable.

#### 2.1.3. Estimation of intraparticle transport limitations

Intraparticle transport limitations in the catalyst pellets are accounted for by the effectiveness factors $\eta_j$ in Eqs. (2c) and (2d). They are calculated from the Thiele modulus assuming $CO_2$ to be the limiting species as $H_2$ diffuses much faster. This approach was also adopted by Sudiro et al. (2010). For spherical pellets and first-order behavior the effectiveness factor is given by, among others, Renken et al. (2012, p. 89) as

$$\eta = \frac{3}{\phi}\left(\frac{1}{\tanh\phi} - \frac{1}{\phi}\right) \tag{7}$$

where $\phi$ is the Thiele modulus here defined as

$$\phi = \frac{d_p}{2}\sqrt{\frac{M_{CO_2} r_{CO_2}^{(V)}}{D_{CO_2}^{(eff)} \rho_{CO_2}}}. \tag{8}$$

The effective diffusivity, $D_{CO_2}^{(eff)}$, is computed using the Bosanquet formula:

$$\frac{1}{D_{CO_2}^{(eff)}} = \frac{1}{D_{c,CO_2}^{(eff)}} + \frac{1}{D_{Kn,CO_2}^{(eff)}}. \tag{9}$$

Herein, $D_{c,CO_2}^{(eff)}$ is the effective molecular diffusion coefficient in the continuum regime estimated with Wilke's approach:

$$D_{c,CO_2}^{(eff)} = \frac{\varepsilon_p}{\tau^2} \frac{1-\omega_i}{M \sum_{k=1,k\neq i}^{n_s} \frac{\omega_i}{M_k D_{ik}}}, \tag{10}$$

and $D_{Kn,CO2}^{(eff)}$ is the effective Knudsen diffusion coefficient:

$$D_{Kn,CO2}^{(eff)} = \frac{\varepsilon_p}{\tau^2} \frac{d_p}{3} \sqrt{\frac{8 R_u T}{\pi M_{CO_2}}}. \tag{11}$$

The influence of the porous pellet is expressed by the parallel pore model via the pellet porosity $\varepsilon_p$ and the tortuosity $\tau$. All quantities in Eqs. (8)–(11) are evaluated along the reactor axis at the corresponding temperature, pressure, and composition in the bulk phase.

We note that this approach provides only an estimation of the transport limitations within the catalyst pellets, and more involved models should be applied for accurate predictions. Nevertheless, this simple approach gives reasonable results regarding the overall reactor performance for practical design, compared to the results of Schlereth and Hinrichsen (2014, Fig. 6c). A typical profile of the effectiveness factors along the reactor axis is shown in Fig. A1 in Appendix A.

#### 2.1.4. Pressure drop and heat transfer correlations

The permeability, $K$, and the Forchheimer coefficient, $c_F$, in Eq. (2b) are calculated with the correlation of Eisfeld and Schnitzlein (2001) that accounts for the pressure drop of an infinite packed bed and the contribution of wall-friction. The latter becomes substantial for slim tubes, which are usually applied for highly exothermic reactions. For a randomly packed bed the permeability and Forchheimer coefficient read

$$K = \frac{\varepsilon^3 D_p^2}{154 A_w^2 (1-\varepsilon)^2} \tag{12}$$

$$c_F = \frac{B_w}{A_w} \frac{\varepsilon^3 D_p}{(1-\varepsilon)}. \tag{13}$$

Here, $A_w$ and $B_w$ are coefficients depending on the tube-to-particle-diameter ratio $N = D_t/D_p$:

$$A_w = 1 + \frac{2}{3N(1-\varepsilon)}, \tag{14}$$

$$B_w = \left(\frac{1.15}{N^2} + 0.87\right)^2. \tag{15}$$

Eqs. (12)–(15) are valid for $N \geq 1.6$ and a wide range of Reynolds numbers.

The effective wall heat transfer coefficient, $U_w^{(eff)}$, in Eq. (2d) results from the cross-sectional averaging of the temperature (Rasmuson et al., 2014, Section 5.2.5). It is a sequential combination of the wall heat transfer resistance because of the increasing bed porosity close to the wall, and the radial heat transfer resistances within the catalyst bed. The final expression yields

$$\frac{1}{U_w^{(eff)}} = \frac{1}{\alpha_w} + c\frac{D_R}{\lambda_r^{(eff)}} \tag{16}$$

where $c$ is a factor depending on the reactor Biot-number. Using a two-dimensional pseudo-homogeneous model, Dixon (1996) derived the following equation for the factor $c$:

$$c = \frac{1}{6}\frac{Bi_R + 3}{Bi_R + 4} \tag{17}$$

where $Bi_R = \alpha_w D_t/(2\lambda_r^{(eff)})$ is the reactor Biot-number. In earlier studies Beek (1962), Froment (1962), and Finlayson (1971) used $c = 1/8$ which is, however, only valid in the case of small Biot-numbers ($Bi_R \to 0$). Finlayson (1971) and Villadsen and Michelsen (1978, p. 248) also used $c = 1/6$ for infinite Biot-numbers ($Bi_R \to \infty$). Eq. (17), however, provides accurate results over the whole range of Biot-numbers, and is thus used in this study.

A comprehensive summary of the estimation of the wall heat transfer coefficient $\alpha_w$ and the effective radial thermal conductivity $\lambda_r^{(eff)}$ is given by Tsotsas (2006a,b).

#### 2.1.5. Calculation of the fluid and mixture properties

The temperature-dependent fluid properties of pure species, such as dynamic viscosity, specific heat, and thermal conductivity, are computed from well-established correlations summarized by Kleiber and Joh (2006). Given the pure species properties and the mixture composition, the mixture viscosity and thermal conductivity are computed using well-known mixing rules, see for example Bird et al. (2007, Sections 1.4 and 9.3). The mixture specific heat is computed as weighted average of the pure species specific heats and their corresponding mass fraction:

$$c_p = \sum_{i=1}^{n_s} \omega_i c_{p,i}. \tag{18}$$

Similarly, the average molecular weight of the mixture is calculated as molar weighted average:

$$M = \sum_{i=1}^{n_s} x_i M_i. \tag{19}$$

### 2.2. Description of the dimensionless model and the SNO-method

In order to reduce the number of parameters, and to identify relevant dimensionless groups, we scale the dimensional model Eqs. (2a)–(2d) and the boundary conditions (3a). Therefore, we define the following dimensionless variables:

$$\Theta = \frac{T - T_0}{T_0}\gamma, \quad \Theta_c = \frac{T_c - T_0}{T_0}\gamma, \quad \gamma = \frac{E_a}{R_u T_0} \tag{20a}$$

$$\hat{z} = \frac{z}{L}, \quad \hat{v}_s = \frac{G}{\rho_0}, \quad \hat{p} = \frac{p}{G}\frac{\rho_0}{\mu_0}\frac{K}{L} \tag{20b}$$

$$\hat{G} = \frac{G}{G_0}, \quad \hat{\rho} = \frac{\rho}{\rho_0}, \quad \hat{\mu} = \frac{\mu}{\mu_0}, \quad \hat{c}_p = \frac{c_p}{c_{p,0}} \tag{20c}$$

$$\hat{M}_i = \frac{M_i}{M_0}, \quad \hat{\eta}_j = \frac{\eta_j}{\eta_0}, \quad \hat{r}_j^{(V)} = \frac{r_j^{(V)}}{r_0^{(V)}}, \quad \Delta\hat{H}_R = \frac{\Delta H_R}{\Delta H_{R,0}}. \tag{20d}$$

Here, the index 0 indicates quantities at the reactor inlet. Replacing the dimensional variables in Eqs. (2a)–(2d) according to Eqs. (20a)–(20d) yields the following set of dimensionless equations:

$$\frac{d\hat{G}}{d\hat{z}} = 0 \tag{21a}$$

$$\frac{d\hat{p}}{d\hat{z}} = -\hat{\mu}\hat{v}_s - Re\hat{\rho}\hat{v}_s^2 \tag{21b}$$

$$\frac{d\omega_i}{d\hat{z}} = \hat{M}_i Da_I \sum_{j=1}^{n_r} \nu_{ij}\hat{\eta}_j \hat{r}_j^{(V)}, \quad i = 1 \ldots n_s \tag{21c}$$

$$\hat{c}_p \frac{d\Theta}{d\hat{z}} = Da_I B \sum_{j=1}^{n_r} \left(-\Delta\hat{H}_R\right)_j \hat{\eta}_j \hat{r}_j^{(V)} - St(\Theta - \Theta_c) \tag{21d}$$

subject to the dimensionless boundary conditions:

$$\hat{G}(\hat{z} = 0) = 1 \tag{22a}$$

$$\hat{p}(\hat{z} = 0) = \hat{p}_0 \tag{22b}$$

$$\omega_i(\hat{z} = 0) = \omega_{i,0} \tag{22c}$$

$$\Theta(\hat{z} = 0) = 0. \tag{22d}$$

The introduced dimensionless groups in Eqs. (21a)–(21d) are summarized in Table 1.

The most important parameter regarding thermal optimization is the *Semenov number* (Semenov, 1928), *Se*, because it provides an intuitive and illustrative representation of the thermal behavior of the reactor. The Semenov number takes low values ($Se \to 0$) for high cooling rates or low heat production rates representing isothermal reactors. In the opposite case, meaning low cooling rates or high heat production rates, the Semenov number takes high values ($Se \to \infty$) and thus describes adiabatic behavior. A moderate Semenov number characterizes a non-isothermal reactor, and its value uniquely determines the axial temperature profile within the reactor as shown in Fig. 3. Consequently, we use the Semenov number within the SNO-method to identify optimal temperature profiles regarding kinetic *and* thermodynamic limitations.

**Table 1**
Summary of dimensionless parameters.

| Parameter | Symbol | Definition | Interpretation/ratio |
|---|---|---|---|
| Arrhenius number | $\gamma$ | $E_a/(R_u T_0)$ | Activation energy/thermal energy |
| Heat production potential | $B$ | $-\Delta H_{R,0}\gamma/(M_0 c_{p,0} T_0)$ | Heat production/thermal storage capacity |
| 1st Damköhler number | $Da_I$ | $M_0\eta_0 r_0^{(V)} L_R/G_0$ | Reaction rate/convective transport rate |
| Stanton number | $St$ | $4U_{w,0}^{(eff)} L_R/(G_0 c_{p,0} D_t)$ | Cooling rate/convective transport rate |
| Reynolds number | $Re$ | $GK/(\mu_0 c_F)$ | Convective momentum transport rate/viscous momentum transport rate |
| Semenov number | $Se$ | $Da_I B/St$ | Heat production rate/cooling rate |

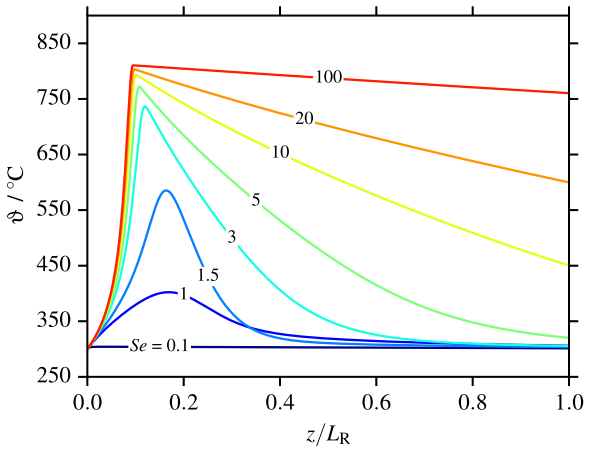


**Fig. 3.** Axial temperature profiles for various Semenov numbers; $\vartheta_0 = \vartheta_c = 300$ °C, $p_0 = 10$ bar(1 MPa), $H_2{:}CO_2 = 4{:}1$, $D_t = 25$mm, $L_R = 0.5$ m, $G = 1.0$ kg m$^{-2}$, $GHSV = 15\,500$ h$^{-1}$ (NTP), ($\gamma = 14.8$, $B = 141.0$, $Da_I = 0.21$).

Further, the explicit definition of the Semenov number (see Table 1) allows us to identify the key parameters for thermal optimization of FBRs:

$$Se = \underbrace{\frac{D_t}{4U_{w,0}^{(eff)}}}_{\text{thermal design}} \underbrace{\frac{\eta_0 r_0^{(V)}(-\Delta H_{R,0})}{T_0}\frac{E_a}{R_u T_0}}_{\text{reaction and process conditions}}. \tag{23}$$

From Eq. (23) it is seen that, the tube diameter, $D_t$, and the heat transport properties of the packed bed, here represented by the effective wall heat transfer coefficient $U_w^{(eff)}$, influence the thermal behavior, and allow thermal optimization of the reactor from an engineering perspective. In addition, different catalyst materials and shapes can be applied to influence the Semenov number. In this study we focus on the tube diameter and the effective wall heat transfer coefficient.

Another important parameter is the 1*st Damköhler number*, representing the length of the reactor, because it mainly influences the final methane-yield.

### 2.3. Numerical solution algorithms

#### 2.3.1. Integration of the governing differential equations

Eqs. (2a)–(2d) and (21a)–(21d) are implemented in Python[1] and integrated numerically along the reactor axis subject to the inlet boundary conditions (3) and (22), respectively, using the ODEPACK library by Hindmarsch and Stepleman (1983). All dimensional and dimensionless mixture properties, such as density, viscosity, specific heat, thermal conductivity, and molar weight, as well as the mixture velocity, pressure, reaction rate, reaction heat, and the overall wall heat transfer coefficient are updated after each integration step.

#### 2.3.2. Computation of optimal Semenov numbers and temperature profiles

As mentioned above, the optimal temperature profiles are identified by an optimal Semenov number, $Se_{opt}$, that is computed from

$$Se_{opt} = \arg\max_{Se \in \mathcal{R}} \{Y_{CH_4}(Se)\} \tag{24}$$

subject to

$$\max T \le T_{lim} \tag{25}$$

[1] A versatile general-purpose high-level programming language. For more information see www.python.org

and subject to Eqs. (21a)–(21d). Eqs. (24) and (25) are solved numerically using the algorithm of Broyden, Fletcher, Goldfarb, and Shanno (BFGS) (Nocedal and Wright, 2006, p. 136) for unconstrained problems ($T_{lim} \to \infty$), and the one of Kraft (1988) for constrained problems.

### 2.4. Influence of interfacial mass and heat transfer

To justify the use of a pseudo-homogeneous model, we estimate the influence of interfacial mass and heat transfer on the axial temperature and concentration profiles using *Mears' criteria*, evaluated at 300 °C and 10 bar (1 MPa):

$$\frac{-r_{CO2,eff}^{(V)} D_p}{\beta_{CO2} c_{CO2,g}} = 0.045 \le 0.3, \tag{26a}$$

$$\frac{\sum_{j=1}^{n_R} \eta_j r_j^{(V)}(-\Delta H_{R,j}) D_p}{\alpha T} = 0.3 \le 0.3. \tag{26b}$$

The mass and heat transfer coefficients $\beta_{CO2} = 6.5$ cm s$^{-1}$ and $\alpha = 1863$ W m$^{-2}$ K$^{-1}$ are calculated using the correlation of Wakao and Kaguei (1982) (see Appendix C). The remaining parameters are listed in Table 2.

Eq. (26a) indicates that interfacial mass transfer is negligible for the $CO_2$-methanation in the considered parameter range. Interfacial heat transfer, however, does have a slight influence. Therefore, we compare the axial temperature and concentration profiles for typical reaction conditions, as considered in this study, computed with the pseudo-homogeneous and a heterogeneous model in Appendix C. The results indicate that the temperature difference between the pseudo-homogeneous and the heterogeneous model is at most about 20 K. Thus, we use the pseudo-homogeneous model in our following computations to reduce computational cost of the optimization.

### 2.5. Validation of the pseudo-homogeneous model

In order to verify the described model and to validate the kinetic model of Lunde and Kester (1974), the dimensional model is used to simulate the isothermal experiments of Schoder et al. (2013) who measured the performance of a 5 wt% $Ru/ZrO_2$ catalyst in a Sabatier process. They used an isothermal and isobaric 0.14 m long and 12 mm in diameter tubular reactor loaded with 1 ml diluted catalyst powder ($0.5\,\text{mm} \le D_p \le 1\,\text{mm}$). The bed porosity is estimated to be 40%. To account for the different metal loading of the catalysts (Lunde and Kester: 4.3 mg cm$^{-3}$ Ru; Schoder et al.: 14.1 mg cm$^{-3}$ Ru, assuming a bulk density of 1.41 g cm$^{-3}$), the kinetic model of Lunde and Kester (1974), Eq. (6), has been multiplied by a factor of 3.3.

Fig. 4 shows a comparison of the $CO_2$-conversion for various temperatures and pressures at $GHSV = 6000$ h$^{-1}$ (NTP) and molar feed ratio $H_2{:}CO_2 = 4{:}1$ diluted in 50% nitrogen. Fig. 4a demonstrates that the adapted kinetic model accounts well for the

**Table 2**
Default dimensional parameters used in the computations.

| Parameter | Symbol | Value |
|---|---|---|
| Tube diameter | $D_t$ | 25 mm |
| Gas load | $G$ | 1 kg m$^{-2}$ s |
| Molar feed ratio | $H_2{:}CO_2$ | 4:1 (undiluted) |
| Bed porosity | $\varepsilon$ | 0.4 |
| Pellet diameter | $D_p$ | 3 mm |
| Pellet porosity | $\varepsilon_p$ | 0.5 |
| Pellet tortuosity | $\tau$ | 3 |
| Average pore diameter | $d_p$ | 50 nm |
| Pellet thermal conductivity | $\lambda_p$ | 5 W m$^{-1}$ K$^{-1}$ |

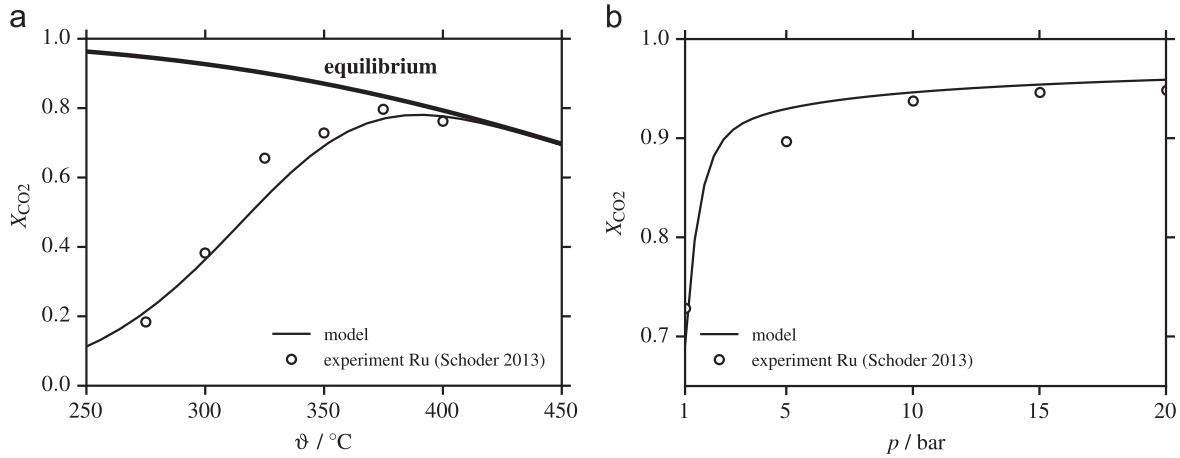


**Fig. 4.** Comparison of the $CO_2$-conversion computed with the described one-dimensional model and experimental data by Schoder et al. (2013) for (a) varying temperature at 1 bar (0.1 MPa), and (b) varying pressure at 350 °C (isothermal catalyst bed). $D_t = 12$ mm, $L_R = 0.14$ m, $GHSV = 6000\ h^{-1}$ (NTP), molar feed ratio $H_2$: $CO_2 = 4:1$ in 50% nitrogen.

physical behavior and provides good accuracy in the whole temperature range. Further, the model also compares well to the experimental data for high pressures up to 20 bar (2 MPa) although Lunde and Kester (1974) measured solely at atmospheric conditions. We note that the extrapolation of kinetic models should be handled with caution, however, the model fits well to the experimental results.

## 3. Thermal optimization of the Sabatier process

### 3.1. Prediction of optimal temperature profiles

Here, we apply the dimensionless model (21a)–(21d) to investigate the potential of thermal optimization of the Sabatier process in single-stage FBRs, and to predict optimal temperature profiles. As explained in Section 2.2 the optimal temperature profiles, which balance kinetic and thermodynamic limitations, are identified by an optimal Semenov number $Se_{opt}$ computed from Eqs. (24) and (25). If not stated otherwise we use the default dimensional parameters summarized in Table 2. The reactor length is set by the Damköhler number, and the effective wall heat transfer coefficient is set by the Semenov number. Further, in this study, we consider only cases where the cooling temperature $T_c$ is constant along the reactor axis and equal to the inlet temperature $T_0$.

Fig. 5 shows the results of a parametric study in the yield–temperature plane for various Semenov and Damköhler numbers for a Sabatier process with inlet temperature $\vartheta_0 = \vartheta_c = 300$ °C and an inlet pressure $p_0 = 10$ bar (1 MPa). The bold black curve indicates the equilibrium yield at the inlet pressure; the thin solid curves represent actual temperature profiles within the reactor for a specific $Se$, and the dotted curves indicate lines of constant $Da_I$.

It is seen that the temperature increases with the Semenov number and relatively sharp temperature peaks occur for large Semenov numbers. Further, for Semenov numbers larger 4, the temperature profile peaks rapidly until it coincidences with the equilibrium line. This type of profile indicates a runaway of the reactor where the temperature increases uncontrollably.

Following the lines of constant $Da_I$ we see that the methane-yield increases rapidly with increasing Semenov number and exhibits a maximum. Afterwards it decreases again and approaches the thermodynamic limit. At the left side of the maximum kinetic effects limit the methane-yield, whereas on the right side of the maximum thermodynamic effect become significant and thus limit the achievable methane-yield. This means that there exists a specific Semenov

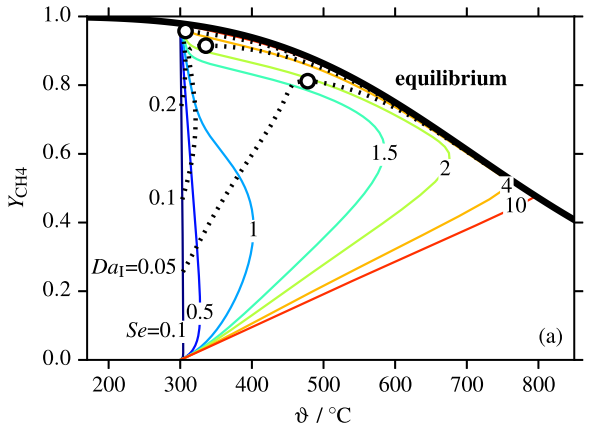


**Fig. 5.** $Se$- (–) and $Da_I$-isolines (···) for the Sabatier process in the yield–temperature plane. The maximal yield is indicated by circles (○). $\vartheta_0 = \vartheta_c = 300$ °C, $p_0 = 10$ bar (1 MPa) ($\gamma = 14.8$, $B = 141.0$).

number, $Se_{opt}$, that for a given $Da_I$ results in maximal methane-yield. This translates to the dimensional space as follows: for a given reactor length $L_R$ there exists a specific axial temperature profile that maximizes the methane-yield and thus intensifies the process.

Fig. 6 shows the methane-yield and the space-time yield at the reactor outlet as a function of the Semenov number for the same reaction conditions as in Fig. 5. Again, it is seen in Fig. 6a that the methane-yield increases rapidly with increasing Semenov number and, after a maximum, decreases for large Semenov numbers. For large Damköhler numbers the methane-yield is generally higher because of larger average contact times, and the maximum changes towards a broader plateau. The behavior of the STY, shown in Fig. 6b, is similar to the one of the methane yield, however, the STY is generally larger for small Damköhler numbers because of the smaller reactor volume. The maximal space–time yield, however, is obtained at similar Semenov numbers as the maximal methane-yield.

The complex interplay between the space–time yield and the methane-yield is shown in Fig. 7. Here, we plot the maximal attainable space–time yield for a fixed $Da_I$ over the maximal attainable methane-yield for the same value of $Da_I$. The STY increases with increasing methane-yield until a methane-yield of 45%. For higher methane-yields, the STY decreases again, especially for methane-yields larger 80%. Comparison with Fig. 5 leads to the conclusion that maximal space–time yields for $CO_2$-methanation are obtained in adiabatic

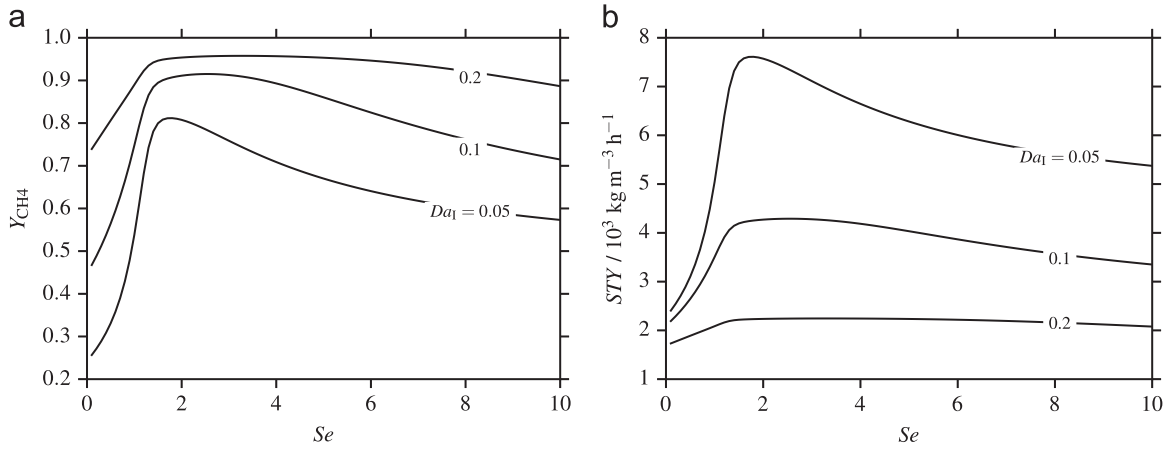


**Fig. 6.** Methane-yield (a) and space–time yield (b) as a function of $Se$ for varying $Da_I$; $\vartheta_0 = \vartheta_c = 300$ °C, $p_0 = 10$ bar (1 MPa), $H_2$:$CO_2$=4:1, ($\gamma$=14.8, $B$=141.0).

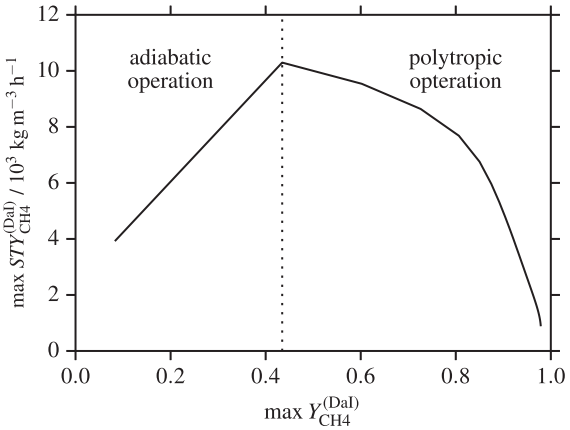


**Fig. 7.** Dependence of maximal attainable space–time yield for given methane-yield at constant $Da_I$ (Pareto front); $\vartheta_0 = \vartheta_c = 300$ °C, $p_0 = 10$ bar (1 MPa), $H_2$:$CO_2$=4:1, ($\gamma$=14.8, $B$=141.0).

**Table 3**
Comparison of the final methane-yield for various Semenov and Damköhler numbers. Stars indicate the optimal Semenov numbers for maximal methane-yield at given Damköhler number. $\vartheta_0 = \vartheta_c = 300$ °C, $p_0 = 10$ bar (1MPa), $H_2$:$CO_2$=4:1, ($\gamma$=14.8, $B$=141.0).

| $Da_I = 0.05$ : $Se$ | **0.1** | **1** | **1.76*** | **4** | **100** |
|---|---|---|---|---|---|
| **Methane-yield** | 0.24 | 0.54 | 0.81 | 0.71 | 0.45 |
| **Normalized yield** | 1.0 | 2.3 | 3.4 | 3.0 | 1.9 |
| $Da_I = 0.10$ : $Se$ | **0.1** | **1** | **2.55*** | **4** | **100** |
| **Methane-yield** | 0.45 | 0.74 | 0.92 | 0.89 | 0.45 |
| **Normalized yield** | 1.0 | 1.6 | 2.0 | 2.0 | 1.0 |

reactors in which equilibrium is obtained directly at the reactor outlet. In this study, however, these outlet conditions are associated with low yields of 45%, and high temperatures that are not tolerable for sustainable catalyst lifetime.

Table 3 shows the methane-yield and the normalized methane-yield for two Damköhler numbers and various Semenov numbers including isothermal ($Se = 0.1$), adiabatic ($Se = 100$), sub- and super-optimal, as well as optimal Semenov numbers; the reaction conditions correspond to the one in Figs. 5 and 6. For $Da_I = 0.05$, the optimal temperature profile gives a 3.4 times higher methane-yield than an isothermal reactor of the same length, and a 1.8 time higher methane-yield than an adiabatic reactor of the same length. Further, the yield is relatively high even at this small Damköhler number. The effect decreases for $Da_I = 0.1$, however, the improvement is still twofold compared to isothermal and adiabatic reactors.

These results demonstrate the high potential of thermal optimization that lie the Sabatier process and show that high yields can be achieved in optimized single-stage FBR.

### *3.2. Influence of the inlet temperature on the optimal Semenov number*

As temperature is the key parameter for the kinetic and thermodynamic behavior of a reaction system, we here investigate the influence of the inlet temperature on the optimal Semenov numbers. Fig. 8 shows optimal Semenov numbers as a function of the Damköhler number for various inlet temperatures computed from Eqs. (24) and (25). Again, in this study we consider only cases where the cooling temperature is equal to the inlet temperature.

Fig. 8a shows optimal Semenov numbers for unconstrained conditions, i.e., no limit on the maximal temperature is set. Regardless of the inlet temperature $T_0$, adiabatic conditions ($Se \to \infty$) are preferable for short reactors. The value of the optimal Semenov numbers then decreases rapidly with increasing Damköhler number to values ranging from 2 to 4. For larger Damköhler numbers the optimal Semenov numbers increase again, especially for low inlet temperatures, to prevent kinetic limitations at the end of the reactor. Further, Fig. 8a can be interpreted in a way that regions above a curve represent thermodynamically limited conditions, and regions below the curve kinetically limited conditions. States lying on the curves optimally balance kinetic and thermodynamic conditions.

Nevertheless, the optimal temperature profiles in Fig. 5 contain high temperatures up to 700 °C that commonly lead to accelerated catalyst deactivation. Consequently, we also computed optimal Semenov numbers for a maximal temperature of $\vartheta_{lim} = 550$ °C that was also reported as temperature limit by Schaaf and Grünig (2014). The results are shown in Fig. 8b. Similar to the unconstrained case adiabatic conditions are preferable for short reactors. The values then rapidly decrease with increasing Damköhler number to approximately 1.4 and remain at this value, independent of the inlet temperature. Here, regions above the curves represent intolerable conditions because of the temperature limit, whereas regions below the curves still represent kinetically limited conditions as in the unconstrained case. This means that, if temperature limitations apply, high yields can only be obtained at the cost of small tube diameters if the effective overall heat

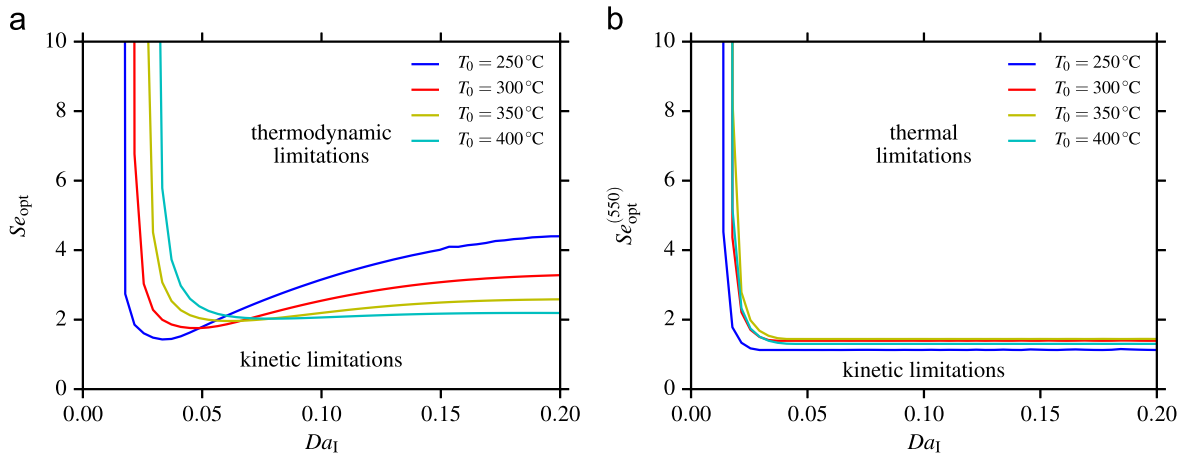


**Fig. 8.** Optimal Semenov numbers for maximized methane-yield as a function of the Damköhler number and (a) unconstrained conditions, and (b) a temperature limit of 550 °C.

transfer coefficient cannot be increased by other means such as high gas loads or structured packings.

The influence of the pressure on the optimal Semenov numbers is small compared to the one of the temperature, and the results are shown in Figs. 10 and 11 in Appendix B.

### 3.3. Case study of single-stage multitubular FBR for $CO_2$-methanation

In this small case study we briefly examine whether the optimal Semenov numbers can be realized using a conventional packed bed composed of spherical catalyst pellets. The effective wall heat transfer coefficient is calculated according Eq. (16); the wall heat transfer coefficient, $\alpha_w$, and the effective lateral thermal conductivity of the catalyst bed, $\lambda_r^{(eff)}$, are estimated from reliable correlations summarized by Tsotsas (2006a,b). Here, we assume the thermal conductivity of the pellet to be constant at $\lambda_p = 5\ W\ m^{-1}\ K^{-1}$.

We choose $\vartheta_0 = \vartheta_c = 300\ °C$ and $p_0 = 10$ bar (1 MPa). Further, we require $Da_I = 0.1$ to obtain a methane-yield larger 90% to reduce expensive post-processing. This leads to a bed length of $L_R = 0.25$ m using the definition of the Damköhler number in Table 1 and the dimensional parameters from Table 2. Calculating the effective wall heat transfer coefficient using the correlations from (Tsotsas, 2006a,b) yields $U_w^{(eff)} = 236.6\ W\ m^{-2}\ K$ and a Semenov number $Se \approx 3.2$ that is significantly larger than the optimal Semenov number $Se_{opt} = 2.5$.

The key parameters to adjust the Semenov number regarding reactor design are the tube diameter $D_t$ and the effective wall heat transfer coefficient $U_w^{(eff)}$. For packed beds the latter is most conveniently adjusted by increasing the gas load to increase lateral dispersion. Consequently, we choose a gas load $G = 1.7\ kg\ m^{-2}\ s^{-1}$ and a reactor length $L_R = 0.5$ m, to maintain $Da_I = 0.1$, to achieve the optimal Semenov number $Se = Se_{opt} = 2.5$.

Another option to reach the optimal Semenov number is to maintain the gas load at $1\ kg\ m^{-2}\ s^{-1}$ and decrease the tube diameter to increase the volumetric surface area for heat exchange. The optimal Semenov number of 2.5 is attained for $D_t = 22$ mm.

While the first option allows larger tubes, and thus larger capacities, it also generates a 3.6 times larger pressure drop. In contrast, the second option maintains a low pressure drop but 30% more tubes have to be used to obtain the same capacity as in the first option. Consequently, final design decisions have to be based on specific requirements of a given scenario, and on economic aspects.

In order to obtain the optimal Semenov number for maximal temperatures of 550 °C within the reactor to reduce catalyst stress, $Se = Se_{opt}^{(550)} = 1.4$, five times larger gas loads and reactor lengths are required at a tube diameter of 25 mm. Again, another option is to reduce the tube diameter to 15 mm at a gas load of $1.0\ kg\ m^{-2}\ s^{-1}$. Both options are rather extreme cases and a combination of increased gas loads and smaller tube diameter will probably provide a technically and economically usable design with optimal Semenov number.

## 4. Conclusion and outlook

In this study we have demonstrated that the Semenov number is a reasonable parameter to describe the dilemma between kinetically and thermodynamically limited conditions in highly exothermic reactions such as the Sabatier process. Further, we have shown for the Sabatier process that an optimization of the Semenov number yields optimal temperature profiles in single-stage FBRs that balance kinetic and thermodynamic limitations, and thus lead to high single-pass methane-yields above 90% for typical reaction conditions of 300 °C and 10 bar (1 MPa) as considered in this study. The optimal Semenov numbers depend slightly on the inlet temperature, and strongly on possible thermal requirements of the catalyst. In the unconstrained case, that is without setting an upper bound for the hot spot in the reactor, the optimal temperature profile increases the methane-yield by a factor of two compared to isothermal and adiabatic operation.

Our case study reveals that the optimal Semenov numbers in the unconstrained case can be realized using conventional packed beds by adjusting the tube diameter and the gas load. The realization of optimal Semenov numbers that meet the thermal requirements of common methanation catalysts, however, requires approximately 1.5 times smaller tube diameters or 3 times larger gas loads compared to the unconstrained case, which would increase capital and operational costs.

In addition, using a Pareto approach, we have demonstrated the diverging behavior of single-pass yield and space–time yield for the Sabatier process. Our results reveal that single-pass yields above 80% can only be obtained at the cost of strongly decreasing space–time yields.

The presented SNO-method can readily be transferred to other either exo- or endothermic processes that suffer from the dilemma between kinetic and thermodynamic limitations. The non-dimensional formulation of the problem, resulting in the Semenov number, provides valuable and intuitive insight into the key

parameters influencing the thermal behavior of the process, namely the tube diameter and the effective heat transfer properties of the catalyst bed, and thus forms the foundation for tailored temperature profiles and thermal optimization in fixed-bed reactors. The influence of other parameters on the optimal temperature profile, such as the catalyst and pellet properties, can also be investigated to obtain a more complete view on the optimal Semenov number.

In conclusion the presented results demonstrate, firstly, the value of an easy-to-use method to compute optimal temperature profiles in single-stage fixed-bed reactors, secondly, the high potential of thermal optimization that lies in the Sabatier process, and thirdly, the need for catalyst supports with enhanced heat transport that allow larger tube diameters for highly exothermic processes. Consequently, future research efforts should focus on catalyst supports with improved and tailorable heat transport properties to enable efficient small-scale units for decentralized Chemical Energy Storage.

## Notation

*Roman*

| | |
|---|---|
| $A$ | pre-exponential factor, $s^{-1}\,bar^{-0.125}$ |
| $A_V$ | external solid surface area per unit reactor volume, $m^2\,m^{-3}$ |
| $c_F$ | Forchheimer coefficient, m |
| $c_p$ | mixture specific heat, $J\,kg^{-1}\,K^{-1}$ |
| $D_i^{(m)}$ | molar diffusivity of component $i$ in the mixture, $m^2\,s^{-1}$ |
| $D_c^{(eff)}$ | effective molar diffusivity, $m^2\,s^{-1}$ |
| $D_{kn}^{(eff)}$ | effective Knudsen diffusivity, $m^2\,s^{-1}$ |
| $D_t$ | tube diameter, m |
| $D_p$ | average pellet diameter, m |
| $d_p$ | average pore diameter, m |
| $E_a$ | activation energy, $J\,mol^{-1}$ |
| $G$ | gas load, $kg\,m^{-2}\,s^{-1}$ |
| $GHSV$ | gas hourly space velocity, $m^3\,m^{-3}\,h^{-1}$ |
| $K$ | bed permeability, $m^2$ |
| $K_p$ | pressure-based equilibrium constant, $bar^{-2}$ |
| $L_R$ | reactor length, m |
| $M$ | molar weight, $kg\,mol^{-1}$ |
| $n_s$ | number of species, – |
| $p$ | pressure, Pa |
| $q$ | heat flux, $W\,m^{-2}$ |
| $R_u$ | universal gas constant, $8.314\,J\,mol^{-1}\,K^{-1}$ |
| $r^{(V)}$ | volumetric reaction rate, $mol\,m^{-3}\,s^{-1}$ |
| $STY$ | space–time yield, $kg\,m^{-3}\,h^{-1}$ |
| $T$ | absolute temperature, K |
| $T_c$ | absolute cooling temperature, K |
| $T_{lim}$ | absolute temperature limit, K |
| $T_s$ | solid surface temperature, K |
| $U_w^{(eff)}$ | effective wall heat transfer coefficient, $W\,m^{-2}\,K$ |
| $v_z$ | intrinsic axial velocity, $m\,s^{-1}$ |
| $x$ | mole fraction, – |
| $z$ | axial coordinate, m |

*Greek*

| | |
|---|---|
| $\alpha_p$ | pellet heat transfer coefficient, $W\,m^{-2}\,K^{-1}$ |
| $\alpha_w$ | wall heat transfer coefficient, $W\,m^{-2}\,K^{-1}$ |
| $\beta_p$ | pellet mass transfer coefficient, $m\,s^{-1}$ |
| $\Delta H_R$ | enthalpy of reaction, $J\,mol^{-1}$ |
| $\varepsilon$ | bed porosity, – |
| $\varepsilon_p$ | pellet porosity, – |
| $\lambda_f$ | fluid thermal conductivity, $W\,m^{-1}\,K^{-1}$ |
| $\lambda_r^{(eff)}$ | effective radial thermal conductivity, $W\,m^{-1}\,K^{-1}$ |
| $\lambda_p$ | pellet thermal conductivity, $W\,m^{-1}\,K^{-1}$ |
| $\mu$ | mixture viscosity, $kg\,m^{-1}\,s^{-1}$ |
| $\nu$ | stoichiometric coefficient, – |
| $\vartheta$ | temperature, °C |
| $\vartheta_c$ | cooling temperature, °C |
| $\vartheta_{lim}$ | temperature limit,°C |
| $\tau$ | pellet tortuosity, – |
| $\eta$ | effectiveness factor, – |
| $\rho$ | mixture density, $kg\,m^{-3}$ |
| $\rho_i$ | mass concentration of component $i$, $kg\,m^{-3}$ |
| $\rho_{i,s}$ | solid surface mass concentration of component $i$, $kg\,m^{-3}$ |
| $\omega$ | mass fraction, – |

*Dimensionless*

| | |
|---|---|
| $\hat{c}_p$ | dimensionless specific heat, – |
| $\hat{G}$ | dimensionless gas load, – |
| $\Delta\hat{H}_R$ | dimensionless reaction heat, – |
| $\hat{p}$ | dimensionless pressure, – |
| $\hat{v}_s$ | dimensionless superficial velocity, – |
| $\hat{z}$ | dimensionless axial coordinate, – |
| $\hat{\rho}$ | dimensionless mixture density, – |
| $\hat{\mu}$ | dimensionless mixture viscosity, – |
| $\hat{\eta}$ | dimensionless effectiveness factor, – |
| $\hat{r}^{(V)}$ | dimensionless reaction rate, – |
| $\Theta$ | dimensionless temperature, – |
| $\Theta_c$ | dimensionless cooling temperature, – |
| $\phi$ | Thiele modulus, – |
| $\gamma$ | Arrhenius number, – |
| $n$ | catalyst coefficient, – |
| $B$ | heat production potential, – |
| $Da_I$ | 1st Damköhler number, – |
| $Pr$ | Prandtl number, – |
| $Re$ | Reynolds number, – |
| $Re_p$ | pellet Reynolds number, – |
| $Sc_i$ | Schmidt number of component $i$, – |
| $Se$ | Semenov number, – |
| $Se_{opt}$ | optimal Semenov number, – |
| $St$ | Stanton number, – |
| $X_{CO_2}$ | $CO_2$-conversion, – |
| $Y_{CH_4}$ | methane-yield, – |


## Acknowledgments

This work was supported by German Research Foundation (DFG) within the Research Training Group GRK 1860 “Micro-, meso- and macroporous nonmetallic Materials: Fundamentals and Applications” (MIMENIMA).


## Appendix A. Estimation of intraparticle transport limitations

Here we briefly present the results of the estimation of the intraparticle transport limitations described in Section 2.1.3. Fig. A1 shows the effectiveness factor along the normalized reactor length for the case study presented in Section 3.3. The effectiveness factor decreases rapidly from about 0.4 to 0.05 in the first section of the reactor because the increasing temperature accelerates the reaction and transport limitations become more significant. Afterwards the effectiveness factor increases sharply to about 0.2 because the reactant concentrations drop rapidly due to

high reactions rates. Then it increases slowly to about 0.35 at the reactor outlet.

The Thiele modulus in this case ranges from around 5 at feed conditions to approximately 50 at the location of the highest temperature. The estimated values of the effectiveness factors are in reasonable agreement with the ones computed by Schlereth and Hinrichsen (2014) who applied a detailed transport model in their numerical study.

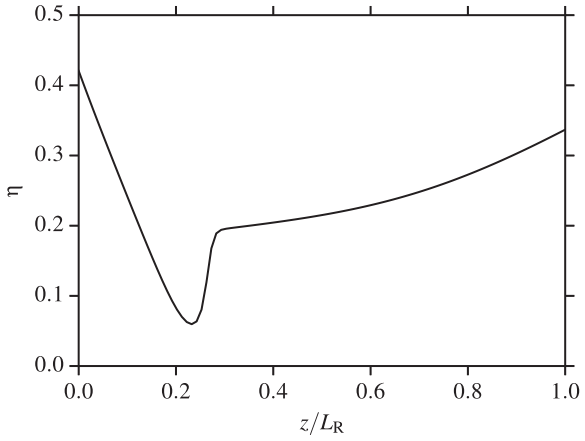


**Fig. A1.** Effectiveness factor along the normalized reactor length for the case study presented in Section 3.3. ($L_R = 0.4$ m, $D_t = 25$ mm, $\vartheta_c = \vartheta_0 = 300$ °C, $p_0 = 10$ bar (1 MPa), $G = 1.7$ kg m$^{-2}$ s$^{-1}$.)

## Appendix B. Influence of the inlet pressure on the optimal Semenov number

Fig. B1 shows the behavior of the *Se*- and $Da_I$-isolines in the yield–temperature plane for feed pressures of 2 bar (0.2 MPa) and 5 bar (0.5 MPa), respectively. Higher pressures lead to slightly higher yields for comparable values of $Da_I$ because of the increased reactant concentrations. Further, thermodynamic limitations are less pronounced at high pressures in the Sabatier process and thus allow higher temperatures to prevent kinetic limitations.

This effect is also seen in Fig. B2 that shows the behavior of the optimal Semenov number for different inlet pressures. Higher pressures shift $Se_{opt}$ to slightly higher values. Nevertheless, the influence of the pressure on the optimal Semenov numbers is rather small compared to the one of the temperature.

## Appendix C. Influence of interfacial transport limitations on the axial temperature and concentration profiles

In order to investigate the influence of interfacial mass and heat transfer on the axial temperature and concentration profiles, we

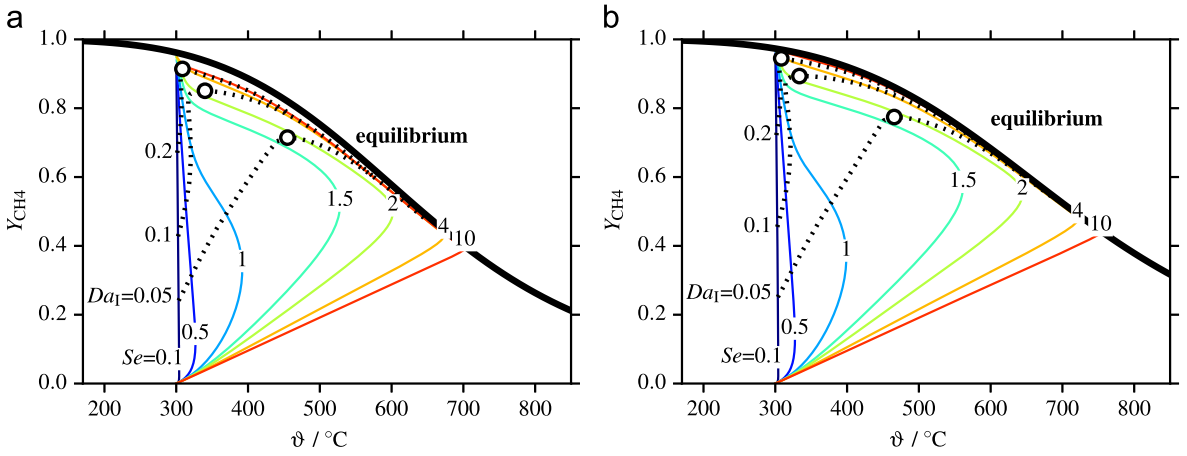


**Fig. B1.** *Se*- (–) and $Da_I$-isolines (···) for the Sabatier process in the yield–temperature plane for (a) $p_0 = 2$ bar (0.2 MPa), and (b) $p_0 = 5$ bar (0.5 MPa). The maximal yield is indicated by circles (○). $\vartheta_0 = \vartheta_c = 300$ °C ($\gamma = 14.8$, $B = 141.0$).

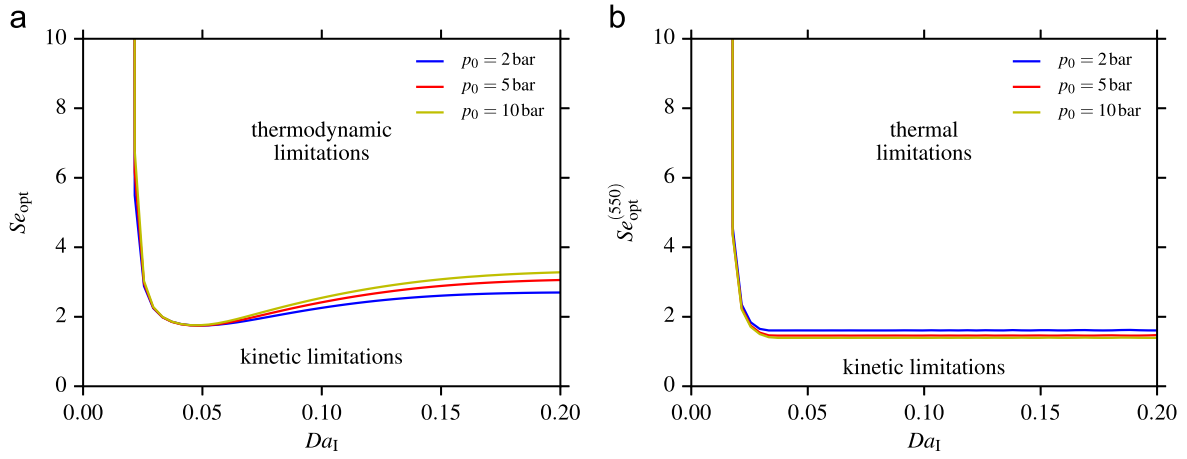


**Fig. B2.** Optimal Semenov numbers for maximized methane-yield as a function of the Damköhler number and (a) unconstrained conditions, and (b) a temperature limit of 550 °C. The feed temperature $\vartheta_c = \vartheta_0 = 300$ °C.

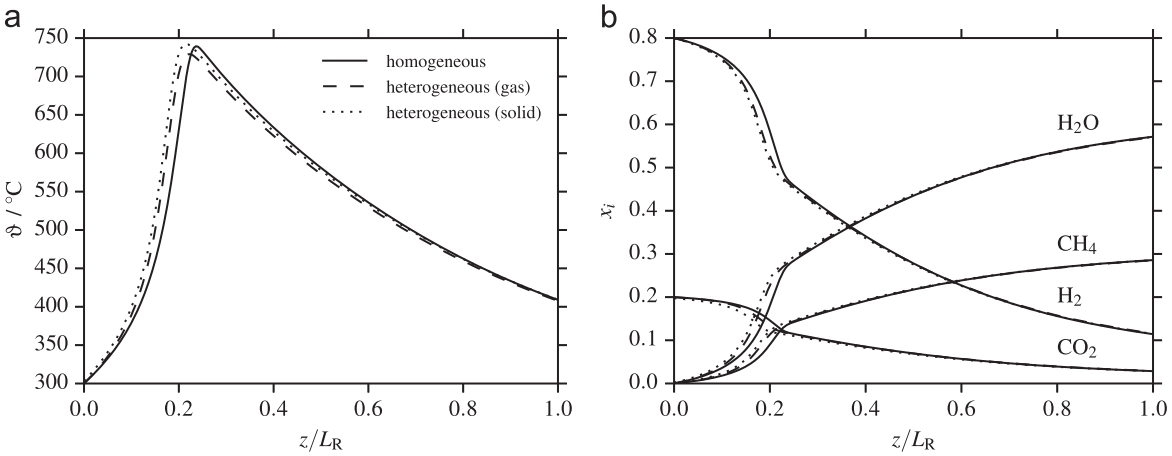


**Fig. C1.** Influence of interpellet mass and heat transfer on (a) the axial temperature profile, and (b) the axial concentration profiles. ($L_R = 0.25$ m, $D_t = 25$ mm, $\vartheta_c = \vartheta_0 = 300$ °C, $p_0 = 10$ bar (1 MPa), $G = 1.0$ kg m$^{-2}$ s$^{-1}$.)

compare the results of the pseudo-homogeneous model, presented in Section 2, with the one of a heterogeneous model. In the heterogeneous case, the governing equations for the gas-phase read

$$G\frac{\mathrm{d}\omega_i}{\mathrm{d}z} = A_V\beta_p(\rho_{i,s}-\rho_i), \quad i = 1\ldots n_s \tag{C.1a}$$

$$Gc_p\frac{\mathrm{d}T}{\mathrm{d}z} = A_V\alpha_p(T_s-T)+\frac{4U_w^{(\mathrm{eff})}}{D_R}(T-T_c), \tag{C.1b}$$

and for the solid phase

$$M_i\sum_{j=1}^{n_r}\nu_{ij}\eta_j r_j^{(V)} = A_V\beta_p(\rho_{i,s}-\rho_i), \quad i = 1\ldots n_s \tag{C.2a}$$

$$\sum_{j=1}^{n_R}\eta_j r_j^{(V)}(-\Delta H_{R,j}) = A_V\alpha_p(T_s-T). \tag{C.2b}$$

The gas-phase equations are completed by Eqs. (2a), (2b), and (4). The boundary conditions are the same as in Eq. (3). The solid-phase equations, Eq. (C.2), are solved iteratively using a Newton–Raphson method at each integration step along the reactor axis.

The external volumetric surface area of the solid catalysts is estimated for spherical pellets as

$$A_V = \frac{6}{D_p}(1-\varepsilon). \tag{C.3}$$

The mass and heat transfer coefficients, $\beta_p$ and $\alpha_p$, are calculated following Wakao and Kaguei (1982):

$$\frac{\beta_p D_p}{D_i} = 2+1.1Sc_i^{0.33}Re_p^{0.5}, \tag{C.4a}$$

$$\frac{\alpha_p D_p}{\lambda_f} = 2+1.1Pr^{0.33}Re_p^{0.5}. \tag{C.4b}$$

The dimensionless groups in Eq. (C.4) are defined as

$$Sc_i = \frac{\mu}{\rho D_i^{(m)}}, \quad Pr = \frac{\mu c_p}{\lambda_f}, \quad Re_p = \frac{\rho v_z D_p}{\mu}. \tag{C.5}$$

Fig. C1 shows a comparison of the axial temperature and concentration profiles computed with the pseudo-homogeneous and the heterogeneous model for the typical process conditions considered in this study. The maximal difference of the pseudo-homogeneous temperature and the gas-phase temperature (Fig. C1a) is about 20 K. The concentration difference between the pseudo-homogeneous and the heterogeneous model, shown in C1b, is negligible. These small differences in temperature and concentration justify the use of the pseudo-homogeneous model for the $CO_2$-methanation with the considered catalyst and parameter-range.

## References


Barbarossa, V., Bassano, C., Deiana, P., Vanga, G., 2013. $CO_2$ Conversion to $CH_4$. In: de Falco, M., Iaquaniello, G., Centi, G. (Eds.), $CO_2$ A Valuable Source of Carbon. Springer, London.

Batista, M.S., Santiago, E.I., Assaf, E.M., Ticianelli, E.A., 2005. Evaluation of the water-gas shift and CO methanation processes for purification of reformate gases and the coupling to a PEM fuel cell system. J. Power Sources 145 (1), 50–54.

Beek, J., 1962. Design of packed catalytic reactors. Adv. Chem. Eng. 3, 203–271.

Bird, R.B., Stewart, W.E., Lightfoot, E.N., 2007. Transport Phenomena, 2nd Edition John Wiley & Sons, New York, NY.

Brooks, K., Hu, J., Zhu, H., Kee, R., 2007. Methanation of carbon dioxide by hydrogen reduction using the Sabatier process in microchannel reactors. Chem. Eng. Sci. 62 (4), 1161–1170.

Centi, G., Perathoner, S., 2009. Opportunities and prospects in the chemical recycling of carbon dioxide to fuels. Catal. Today 148 (3–4), 191–205.

Centi, G., Quadrelli, E.A., Perathoner, S., 2013. Catalysis for $CO_2$ conversion: a key technology for rapid introduction of renewable energy in the value chain of chemical industries. Energy Environ. Sci. 6 (6), 1711.

Dixon, A., 1996. An improved equation for the overall heat transfer coefficient in packed beds. Chem. Eng. Process. Process Intensif. 35 (5), 323–331.

Eisfeld, B., Schnitzlein, K., 2001. The influence of confining walls on the pressure drop in packed beds. Chem. Eng. Sci. 56, 4321–4329.

Finlayson, B.B.A., 1971. Packed bed reactor analysis by orthogonal collocation. Chem. Eng. Sci. 26, 1081–1091.

Freund, H., Sundmacher, K., 2008. Towards a methodology for the systematic analysis and design of efficient chemical processes. Chem. Eng. Process. Process Intensif. 47 (12), 2051–2060.

Froment, G., 1962. Design of fixed-bed catalytic reactors based on effective transport models. Chem. Eng. Sci. 17, 849–859.

Froment, G.F., Bischoff, K.B., Wilde, J.D., 2011. Chemical Reactor Analysis and Design, 3rd Edition John Wiley & Sons, New York, NY.

Gao, J., Wang, Y., Ping, Y., Hu, D., Xu, G., Gu, F., Su, F., 2012. A thermodynamic analysis of methanation reactions of carbon oxides for the production of synthetic natural gas. RSC Adv. 2 (6), 2358.

Gnanamani, M.K., Jacobs, G., Pendyala, V.R.R., Ma, W., Davis, B.H., 2014. Hydrogenation of carbon dioxide to liquid fuels. In: Centi, G., Perathoner, S. (Eds.), Green Carbon Dioxide: Advances in $CO_2$ Utilization. John Wiley & Sons, Hoboken, NJ.

Hindmarsch, A., 1983. ODEPACK, A systematized collection of ODE solvers. In: Stepleman, R.S. (Ed.), Scientific Computing. North-Holland, Amsterdam, NL, pp. 55–64.

Hoekman, S.K., Broch, A., Robbins, C., Purcell, R., 2010. CO2 recycling by reaction with renewably-generated hydrogen. Int. J. Greenh. Gas Control 4 (1), 44–50.

Hu, J., Brooks, K., Holladay, J., Howe, D., Simon, T., 2007. Catalyst development for microchannel reactors for martian in situ propellant production. Catal. Today 125 (1–2), 103–110.

Jürgensen, L., Ehimen, E.A., Born, J., Holm-Nielsen, J.B., 2014. Utilization of surplus electricity from wind power for dynamic biogas upgrading: Northern Germany case study. Biomass Bioenergy 66, 126–132.

Kleiber, M., Joh, R., 2006. Stoffwerte von sonstigen chemisch einheitlichen Flüssigkeiten und Gasen. In: VDI-Wärmeatlas, 10th Edition. Springer, Berlin, pp. Dca1–Dca46 (German).

Kopyscinski, J., Schildhauer, T.J., Biollaz, S., 2010. Production of synthetic natural gas (SNG) from coal and dry biomass-A technology review from 1950 to 2009. Fuel 89 (8), 1763–1783.
Kraft, D., 1988. A Software Package for Sequential Quadratic Programming (DFVLR-FB 88-28). Technical Report, DLR German Aerospace Center-Institute for Flight Mechanics, Köln, Germany.
Krämer, M., Duisberg, M., Stöwe, K., Maier, W.F., Kramer, M., Duisberg, M., Stowe, K., Maier, W.F., 2007. Highly selective CO methanation catalysts for the purification of hydrogen-rich gas mixtures. J. Catal. 251 (2), 410–422.
Leal, A.M., Blunt, M.J., LaForce, T.C., 2013. A robust and efficient numerical method for multiphase equilibrium calculations: application to $CO_2$-brine-rock systems at high temperatures, pressures and salinities. Adv. Water Resour. 62, 409–430.
Liu, Z., Chu, B., Zhai, X., Jin, Y., Cheng, Y., 2012. Total methanation of syngas to synthetic natural gas over Ni catalyst in a micro-channel reactor. Fuel 95, 599–605.
Logist, F., Smets, I., van Impe, J., 2008. Derivation of generic optimal reference temperature profiles for steady-state exothermic jacketed tubular reactors. J. Process Control 18 (1), 92–104.
Lunde, P., Kester, F., 1974. Carbon dioxide methanation on a ruthenium catalyst. Ind. Eng. Chem. Process Des. Dev. 53 (1), 321–330.
Minutillo, M., Perna, A., 2014. Renewable energy storage system via coal hydro-gasification with co-production of electricity and synthetic natural gas. Int. J. Hydrog. Energy 39 (11), 5793–5803.
Moeller, C., Meiss, J., Mueller, B., Hlusiak, M., Breyer, C., Kastner, M., Twele, J., 2014. Transforming the electricity generation of the Berlin-Brandenburg region, Germany. Renew. Energy 72, 39–50.
Mohseni, F., Görling, M., Alvfors, P., 2013. The competitiveness of synthetic natural gas as a propellant in the Swedish fuel market. Energy Policy 52, 810–818.
Nocedal, J., Wright, S.J., 2006. Numerical Optimization. Springer, New York, NY.
Ohya, H., Fun, J., Kawamura, H., Itoh, K., 1997. Methanation of carbon dioxide by using membrane reactor integrated with water vapor permselective membrane and its analysis. J. Membr. Sci. 131 (1–2), 237–247.
Park, E.D., Lee, D., Lee, H.C., 2009. Recent progress in selective CO removal in a $H_2$-rich stream. Catal. Today 139 (4), 280–290.
Parlikkad, N.R., Chambrey, S., Fongarland, P., Fatah, N., Khodakov, A., Capela, S., Guerrini, O., 2013. Modeling of fixed bed methanation reactor for syngas production: operating window and performance characteristics. Fuel 107, 254–260.
Peschel, A., Freund, H., Sundmacher, K., 2010. Methodology for the design of optimal chemical reactors based on the concept of elementary process functions. Ind. Eng. Chem. Res. 49 (21), 10535–10548.
Rasmuson, A., Andersson, B., Olsson, L., Andersson, R., 2014. Mathematical Modeling in Chemical Engineering. Cambridge University Press, Cambridge, UK.
Renken, A., Kiwi-Minsker, L., 2012. Catalytic reaction engineering principles. In: Beller, M., Renken, A., van Santen, R.A. (Eds.), Catalysis: From Principles to Applications. Wiley-VCH, Weinheim, GER, pp. 67–109 (Chapter 4).
Sabatier, P., Senderens, J.B., 1902. New synthesis of methane. Comptes Rendus 134, 514–516.
Schaaf, T., Grünig, J., 2014. Speicherung von elektrischer Energie im Erdgasnetz -Methanisierung von $CO_2$-haltigen Gasen. Chem. Ing. Tech. 86 (4), 476–485.
Schlereth, D., Hinrichsen, O., 2014. A fixed-bed reactor modeling study on the methanation of $CO_2$. Chem. Eng. Res. Des. 92 (4), 702–712.
Schlögl, R. (Ed.), 2013. Chemical Energy Storage. De Gruyter, Berlin.
Schoder, M., Armbruster, U., Martin, A., 2013. Heterogen katalysierte Hydrierung von Kohlendioxid zu Methan unter erhöhten Drücken. Chem. Ing. Tech. 85 (3), 344–352.
Semenov, N., 1928. Zur Theorie des Verbrennungsprozesses. Z. Phys. A Hadron. Nucl. 48, 571–851.
Smets, I., Dochain, D., Impe, J.V., 2002. Optimal temperature control of a steady-state exothermic plug-flow reactor. AIChE J. 48 (2).
Sudiro, M., Bertucco, A., 2010. Synthetic natural gas (SNG) from coal and biomass: a survey of existing process technologies, open issues and perspectives. In: Primoz Potocnik (Ed.), Natural Gas. InTech, Rijeka, pp. 105–127.
Sudiro, M., Bertucco, A., Groppi, G., Tronconi, E., 2010. Simulation of a structured catalytic reactor for exothermic methanation reactions producing synthetic natural gas. Comput. Aided Chem. Eng. 28, 691–696.
Tsotsas, E., 2006a. Wärmeleitung in Schüttschichten. In: VDI-Wärmeatlas, 10th Edition. Springer, Berlin, pp. Dee1–Dee9 (German).
Tsotsas, E., 2006b. Wärmeleitung und Dispersion in durchströmten Schüttungen. In: VDI-Wärmeatlas, 10th Edition. Springer, Berlin, pp. Mh1–Mh15 (German).
Varma, A., Morbidelli, M., Wu, H., 2005. Parametric Sensitivity in Chemical Systems. Cambridge University Press, Cambridge, UK (First published 1999).
Villadsen, J., Michelsen, M., 1978. Solution of Differential Equation Models by Polynomial Approximation. Prentice-Hall, Englewood Cliffs, NJ.
Wakao, N., Kaguei, S., 1982. Heat and Mass Transfer in Packed Beds. Routledge, London.
Wang, W., Gong, J., Jinlong, G., Gong, J., 2010. Methanation of carbon dioxide: an overview. Front. Chem. Sci. Eng. 5 (1), 2–10.
Wang, W., Wang, S., Ma, X., Gong, J., 2011. Recent advances in catalytic hydrogenation of carbon dioxide. Chem. Soc. Rev. 40, 3703–3727.